

Fig. S1. Quantification of orientation of hexagonal cells. (A) Orientation of a hexagonal cell is characterized by $\langle \cos 6\theta_i \rangle$ (the average of $\cos 6\theta_i$, where θ_{1-6} represents the angles of the edges belonging to the cell). The PD and AP oriented hexagons are colored blue and yellow, respectively. (A') Hexagonal cells are color-coded by $\langle \cos 6\theta_i \rangle$ in the control wing at 35 hours APF. Nonhexagonal cells are shown in black. The $\langle \cos 6\theta_i \rangle$ map illustrates the segregation of hexagonal cell arrays. (B) Orientation of a cell shape anisotropy, ϕ , is defined by the angle of the longest axis of a fitted ellipse. The angle is defined between 0 and π . (B') Cells shown in A' are color-coded by $\cos \phi$. The segregation of hexagonal cell arrays is not clearly detected. The fly genotype is as described in the legend of Fig. 1.

Fig. S2. Developmental changes in the distribution of inferred tension and the myosin subunit in the wing. (A-E) Patterns of the estimated tension at the stages indicated. In B, the arrows indicate the PD and AP edges. (A'-E') The direction of each edge is classified (e.g. red class I for the PD edges and blue class III for the AP edges) and its estimated tension is plotted against its length. The longest axis of the stress ellipse represents the maximum stress direction of a group of cells. (A''-E'') Images of the wing expressing MRLC-GFP under the control of a promoter of the *MRLC* gene (A''-E'') and a cell shape marker (*D α* -catenin-TagRFP) (A'''-E''') at the stages indicated. The yellow and blue arrowheads indicate the PD and AP edges, respectively. Actin-GFP did not show a strongly biased distribution (data not shown). (A''''-E''') Quantification of the mean signal intensity of MRLC-GFP (bar, left y-axis) and the average length of the edges (line, right y-axis) for each angle class. (F) A wing at 24 hours APF stained for anti-Zipper (myosin heavy chain) and anti-DECadherin. The yellow and blue arrowheads indicate the PD and AP edges, respectively. Zipper is enriched on the PD edges, as is MRLC-GFP. Only a low level of phosphor-myosin was detected (data not shown). (G) The MRLC-GFP signal intensity of each edge (arbitrary units) is plotted against its length in each angular class for data shown in B''. (H) The correlation between myosin and the edge length of the class III edges is shown. The number of samples examined is indicated. Class I, II and IV edges had similar values to class III edges (data not shown). The fly genotypes are as described in the legend of Fig. 1 (A-E,G,H), and *DECadherin-GFP* knock-in (F). Scale bars: 20 μ m (A,A'') and 5 μ m (F).

Fig. S3. Statistical analysis of the angular bias of inferred tension, edge length and MRLC signal intensity. (A) The anisotropy of the MRLC-GFP signal intensity is represented by R_S , $R_S \langle s \rangle e^{i2\theta} = \langle s e^{i2\theta} \rangle - \langle s \rangle \langle e^{i2\theta} \rangle$, where s_{ij} and θ_{ij} ($0 \leq \theta_{ij} < \pi$) are the MRLC-GFP signal intensity and the angle of the contact surface between the i th and j th cells, respectively. R_S decreases if the signal intensity is uncorrelated with respect to the orientation of the edges. The anisotropy of the inferred tension (R_T) and that of the edge length (R_L) were evaluated using the same procedures. See supplementary material Fig. S4 for their statistical significance. (B-B'') The anisotropy of the inferred tension (R_T ; B), the length of the edge (R_L ; B') and the MRLC-GFP signal intensity (R_S ; B'') were plotted [red: wing (data shown in Fig. S2); blue: scutum]. The number of samples examined is indicated. The fly genotype is as described in the legend of Fig. 1.

Fig. S4. Statistical significance of the angular bias of inferred tension, edge length and MRLC signal intensity in the wing. (A) A bootstrap method for evaluating P values. Briefly, starting from the observed data set $\{s_{ij}, \theta_{ij}\}$ (red lines), we generated a bootstrap sample $\{s'_{ij}, \theta_{ij}\}$ by randomly assigning a signal intensity to each edge from $\{s_i\}$ and calculating R_S . Repeating this process 10,000 times, we obtained the distribution for the bootstrap samples (green curve). (B-F'') Data shown in Figs S2, S3 were analyzed to check the statistical significance by evaluating P values using a bootstrap method. We obtained a distribution for R_S , R_T , R_L , and R_S for the observed data for the wing at various developmental stages (lines), plotted together with their distribution for the bootstrap samples (green curves; B-F, B'-F' and B''-F'', respectively). R_T , R_L , and R_S are normalized to their mean values. In each figure, the statistical significance of R is represented by colored lines (red: $P < 0.01$; gray: $P \geq 0.01$). Inset: the directions of R_T , R_L , and R_S are plotted (red: $P < 0.01$; gray: $P \geq 0.01$). R_S was not polarized toward a particular direction (i.e., bias direction θ_S) at 13-14 hours APF (inset in B''). However, at 16.5-23 hours APF, all of the samples were aligned parallel to the PD axis (insets in C'', D''). They then gradually separated at later stages (insets in E'', F''). A bootstrap test indicated that the R_S of almost all of the samples was statistically significant at 16.5-23 hours APF (C'', D''). By contrast, more gray lines representing $P \geq 0.01$ can be seen at other stages (B'', E'', F'').

Fig. S5. Cell junction tension measured by response to laser ablation of single cell contact surface. (A-E') The response to laser cutting of single cell contact surface at the stages indicated was examined as was previously reported (Aigouy et al., 2010; Ishihara and Sugimura, 2012).

Each circle represents one ablated edge plotted on a 2D plane according to its length and direction at different stages. 0 and π correspond to the PD direction (see the number of angle classes). The color of the circle indicates the initial velocity of vertices, which was measured by the displacement of vertices 16 seconds after laser irradiation. For edges of a similar length, displacement was larger at the PD edges than at the AP edges at every stage, except at 13-14 hours APF. These developmental changes were also observed when we quantified the displacement of the vertices at 71 seconds. The number of edges analyzed is shown in the upper right-hand corner. (D',E') The tension of an edge was estimated from image data just before cutting the edge as was done in Ishihara and Sugimura, 2012. The inferred tension plotted against V_{max} of the vertices in wings at 25.5-27.5 hours APF (D') and 30-32 hours APF (E'). The correlation coefficient was 0.80 (25.5-27.5 hours APF) and 0.60 (30-32 hours APF). Results of the analysis at 16.5-18.5 hours APF were published previously (Ishihara and Sugimura, 2012). The fly genotype is as described in the legend of Fig. 1.

Fig. S6. Developmental changes in the anisotropy of global stress. (A) Developmental changes in the inferred normal stress difference $\sigma_A \equiv (\sigma_{xx} - \sigma_{yy})/2$ in control wings. The number of samples examined is indicated. (B) The inferred σ_A plotted against $V_x - V_y$ measured by global ablation of tissue (as in Fig. 2F and Movies 1, 2) for wings at 22 hours APF (red), 26 hours APF (black), 30 hours APF (magenta) and scutum (blue). σ_A was calibrated by the average V_{max} of the vertices after cutting single cell contact surface at corresponding stages. The correlation coefficient was 0.88 with calibration and 0.73 without calibration. The fly genotype was *DEcadherin-GFP* knock-in.

Fig. S7. Anisotropic stress promotes hexagonal packing. (A-D) In addition to cutting the wing by forceps as was done in Figs 3 and 4, we also employed a different way of relaxing tissue stretch; a two-photon laser cut the wing along the anterior cross vein at 23.5-24 hours APF. (A,B) Images of pupal wings at 34.5-35.5 hours APF. In B, the wing was severed by a femtosecond laser at 23.5 hours APF. The percentage of hexagonal cells was: 72.8 % (A) and 57.1 % (B). (C) Quantification of the fraction of hexagonal cells in the control and cut wings. (D) The average value of $\langle \cos 6\theta_j \rangle$ in each wing or wing cut at 23.5-24 hours APF is calculated, and mean \pm s.d. among samples at each developmental stage is plotted. The fly genotype is as described in the legend of Fig. 1.

Fig. S8. Directional bias in stress is crucial for hexagonal packing in a numerical simulation of cell rearrangement. (A) Mechanical processes in a cell. Currently, three processes are considered to underlie pressure and tension: (1) area elasticity, (2) cell adhesion and (3) contraction. Each process can be expressed as a form of potential energy, and minimization of the potential is expected to determine the geometry of the cells. A and L are the area and peripheral length of a cell at the plane of the adherens junction, respectively. l is the length of the contact surface between the cells. (B) Time evolution of the fraction of hexagonal cells for noise intensity $z = 1, 10, 30$ and 50%. The results of the simulations under no stretch, isotropic stretch and horizontal stretch are indicated with green, blue and red lines, respectively. The parameters were set as follows: $\tilde{\sigma}_0 = 0.12$; $\tilde{\Lambda} = 0.04$, and $1/\tau = 0.1$ (see equations S2-2 and S2-5 in Appendix S1). (C) Fractions of hexagonal cells at $t = 2000$ in the numerical simulations are plotted against noise intensity (z) for several values of τ ($\tilde{\sigma}_0 = 0.12$) ($n=8$ for each set of parameters). The results of the simulations under no extrinsic force, isotropic stretch and horizontal stretch are indicated with squares, crosses and circles, respectively. (D,E) Results of simulations under (D) isotropic and (E) horizontal stretch. Left: the newly formed edges through cell-cell intercalation are shown by the magenta lines. Right: angular distribution of the newly formed edges ($n=20$ for each condition).

Fig. S9. The RNAi against *sqh* results in the excess shear deformation of wing cells. (A,B) $\Delta\alpha$ -catenin-TagRFP images of control wing (A) and wing expressing a dsRNA targeting *sqh* that encodes MRLC (B). Yellow dots label corresponding cells. Control and *sqh* RNAi embryos and larvae were raised at 21°C and third instar larvae were switched to 29°C to induce the expression of dsRNA against *sqh*. After 24 hours, white pupae were picked for analysis. Time-lapse imaging was conducted at 21-22 hours APF at 29°C, which corresponds to ~24-25 hours APF at 25°C. In B, excess shear deformation of cells was observed. Over the twenty minutes observation shown (B), and in the 1-hour time-lapse movie (not shown), cell rearrangement was suppressed. When embryos and larvae were raised at 21°C and white pupae were switched to 29°C, excess shear deformation of cells was not observed, and cell rearrangement was biased along the PD axis (refer to the main text). The decrease of MRLC level in the *sqh* RNAi flies was confirmed (data not shown). (C) Mechanical force balance in the *Drosophila* pupal wing.

The intrinsic cell junction tension generated by myosin resists the extrinsic tissue stretch. Inferred tension and myosin signal intensity were negatively correlated with the length of cell contact surface in each angle class (supplementary material Fig. S2A'-E',G,H) as expected from the force-generating property of myosin. On the other hand, the extrinsic force elongates cell contact surfaces. The fly genotypes were *patched-gal4, tubP-gal80^{ts}/sqhp-sqhGFP, UAS-Da-catenin-TagRF*; +/+ (A), and *patched-gal4, tubP-gal80^{ts}/sqhp-sqhGFP, UAS-Da-catenin-TagRF; UAS-sqh dsRNA/+* (B). (C) Scale bar: 20 μ m (B).

Fig. S10. Temporal changes in the anisotropy of local cell stress during hexagonal cell packing. (A,B) The developmental changes in local cell stress. Time-lapse data obtained from 23.5 to 30.5 hours APF were extracted at 3-minute intervals. (A) Each cell is differentially colored by its anisotropy of local cell stress (color bar; a/b in Fig. 5A). The coefficient of variation (CV; the standard deviation/the mean) of the aspect ratio of local cell stress ellipse among cells #1-#4 is indicated at the bottom right of each panel. (B) The aspect ratio of local cell stress ellipse is quantified before and after the PD intercalation of cells. Its CV among four cells that are involved in the PD intercalation is plotted. (C) Balance of the extrinsic forces (blue arrows) and intrinsic contracting forces (pink arrows). An edge with tension T , length l and angle θ contributes to N_{xx} as $\sim Tl\cos^2\theta/a_e$ along the x -axis, where a_e represents an area that the edge supports. It indicates that the tension along the horizontal edges (top) is able to more efficiently counteract the horizontal stretch than the tension of the vertical edges (bottom). It is thus suggested that the PD intercalation of cells (i.e., an increase of the PD edges) lowers the average magnitude of tension on PD edges. The fly genotype is as described in the legend of Fig. 1. Scale bar: 5 μ m (B).

Fig. S11. In *flamingo* (*fmi*) RNAi wing, hexagonal packing proceeded normally until 27.5 h APF, but was disrupted afterwards. (A-A'') The anisotropy of the inferred tension (R_T ; A), the length of the edge (R_L ; A'), and the MRLC-GFP signal intensity (R_S ; A'') were plotted [red: wing (data shown in Fig. S2), magenta: *fmi* RNAi wing]. The number of samples examined is indicated. Inferred tension, myosin localization and cell elongation exhibited normal developmental changes in *fmi* RNAi wings. The standard deviations of the magnitude (c in Fig. 5A) and anisotropy ($a - b$ in Fig. 5A) of inferred local cell stress at 25.5-27.5 hours APF were 0.095 ± 0.013 and 1.10 ± 0.19 in control wing, and they were 0.095 ± 0.013 and 1.17 ± 0.14 in *fmi* RNAi wing. The standard deviation of inferred tension at 25.5-27.5 hours APF was 0.158 ± 0.020 and 0.168 ± 0.014 in the control and *fmi* RNAi wings, respectively. The PD biased localization of myosin was observed in two other conditions, in which PCP was disputed: a homogeneous viable null allele of *prickle* (*prickle¹*) (Gubb et al, 1999) and overexpression of *fat* by *ptc-gal4* (Ma et al., 2003; Matakatsu and Blair, 2004) (data not shown). (B,C) Developmental changes in cell packing and alignment are compared between control and *fmi* RNAi wings. The number of control flies examined is indicated. (B) The fraction of hexagonal cells in control (red) and *fmi* RNAi (magenta) wings. (C) The orientation of the edges of each hexagonal cell is quantified by $\langle \cos 6\theta \rangle$ as in Fig. 1G, and the average of the values among samples is plotted (red: control, and magenta: *fmi* RNAi). Genotype of control fly is as described in the legend of Fig. 1, and that of the *fmi* RNAi fly is *sqhp-sqhGFP, apterous-gal4/sqhp-sqhGFP, UAS-Da-catenin-TagRF*; *UAS-fmi dsRNA/+*.

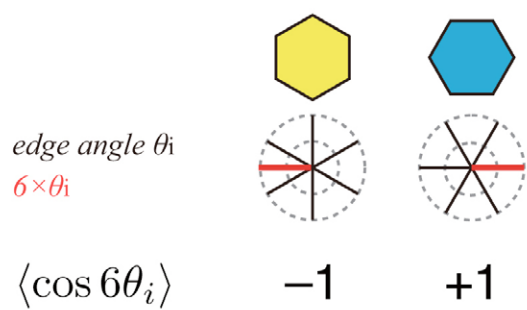
Fig. S12. Summary of tissue mechanics and cell-level dynamics that underlie hexagonal cell packing. (A) Tissue mechanics, cell-level dynamics and hexagonal cell packing in the *Drosophila* pupal wing (Classen et al., 2005; Aigouy et al., 2010; this study). Strong anisotropy of tissue stress is present until early phase II, when the anisotropies of cell junction tension and myosin have started decreasing. This strong tissue stress anisotropy triggers the directional alignment of hexagonal cells along the tissue-stretching direction. (B) Mechanical regulation of hexagonal pattern formation connecting molecular, cellular and tissue (cell-population) dynamics. Arrow 1: Myosin controls the mechanical properties of a cell and generates contracting tension to trigger junction remodeling. Arrow 2: Directional cell rearrangement promotes hexagonal packing. Arrow 3: The stress field (i.e., the maximum stress direction) of a tissue provides directional information for the alignment of individual cells. Arrows 3 and 4: A cell senses the stress field of the tissue and modifies its distribution of myosin.

Movie 1. Ablation of a group of cells in the wing. A wing at 22 hours APF. Anterior is up and proximal is left. Cells at the center were ablated. The anisotropic extension of cell group contour confirmed the PD bias of global stress in the wing. Time label of the movie is: 14", -4", 4", 14", 24", ... , 214" (laser irradiation was at 0 seconds). The fly genotype is *DEcadherin-GFP* knock-in. Scale bar: 20 μ m.

Movie 2. Ablation of a group of cells in the scutum. A scutum at 22 hours APF. Anterior is left. Cells at the center were ablated. Note that the anisotropy in the outward velocity of cells was smaller in the scutum than in the wing (compare Movies 1 and 2). The time label of the movie and fly genotype are as described in the legend of Movie 1. Scale bar: 20 μm .

Movie 3. Temporal dynamics of the inferred tensions. Time-lapse images were taken from 23.5-30.5 hours APF, and data from 25-26 hours APF were extracted at 3-minute intervals. The arrowheads and arrows point to the AP and PD edges, respectively. The fly genotype is as described in the legend of Fig. 1.

A “Orientation of cell contact surface”



B “Orientation of cell shape anisotropy”

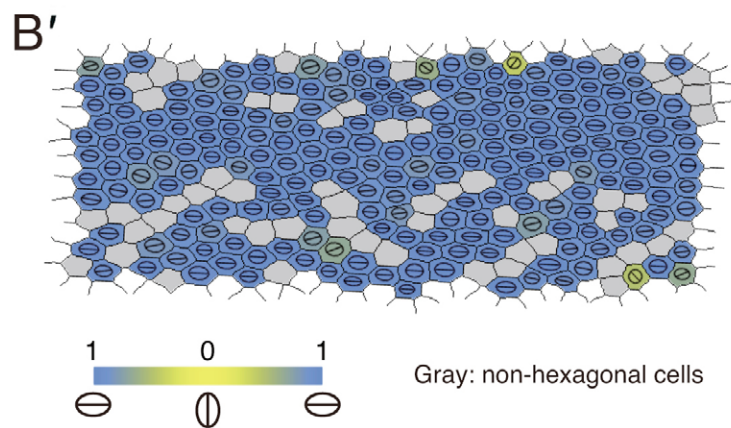
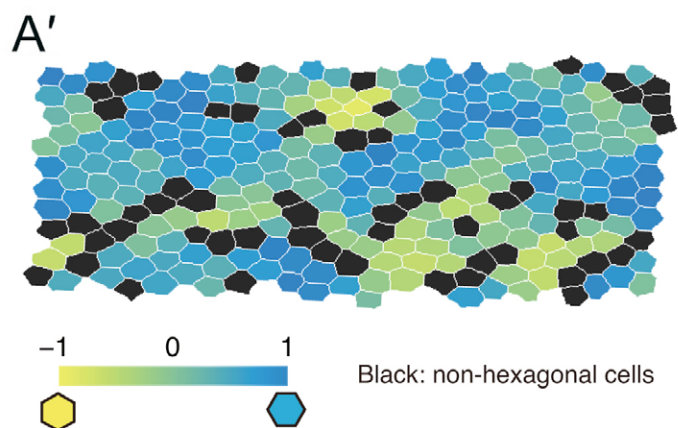
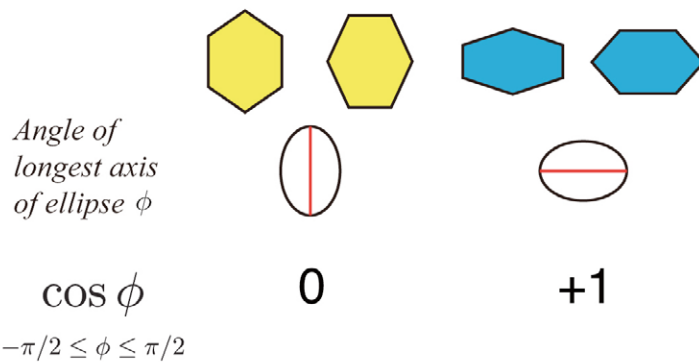


Fig. S1. Quantification of orientation of hexagonal cells.

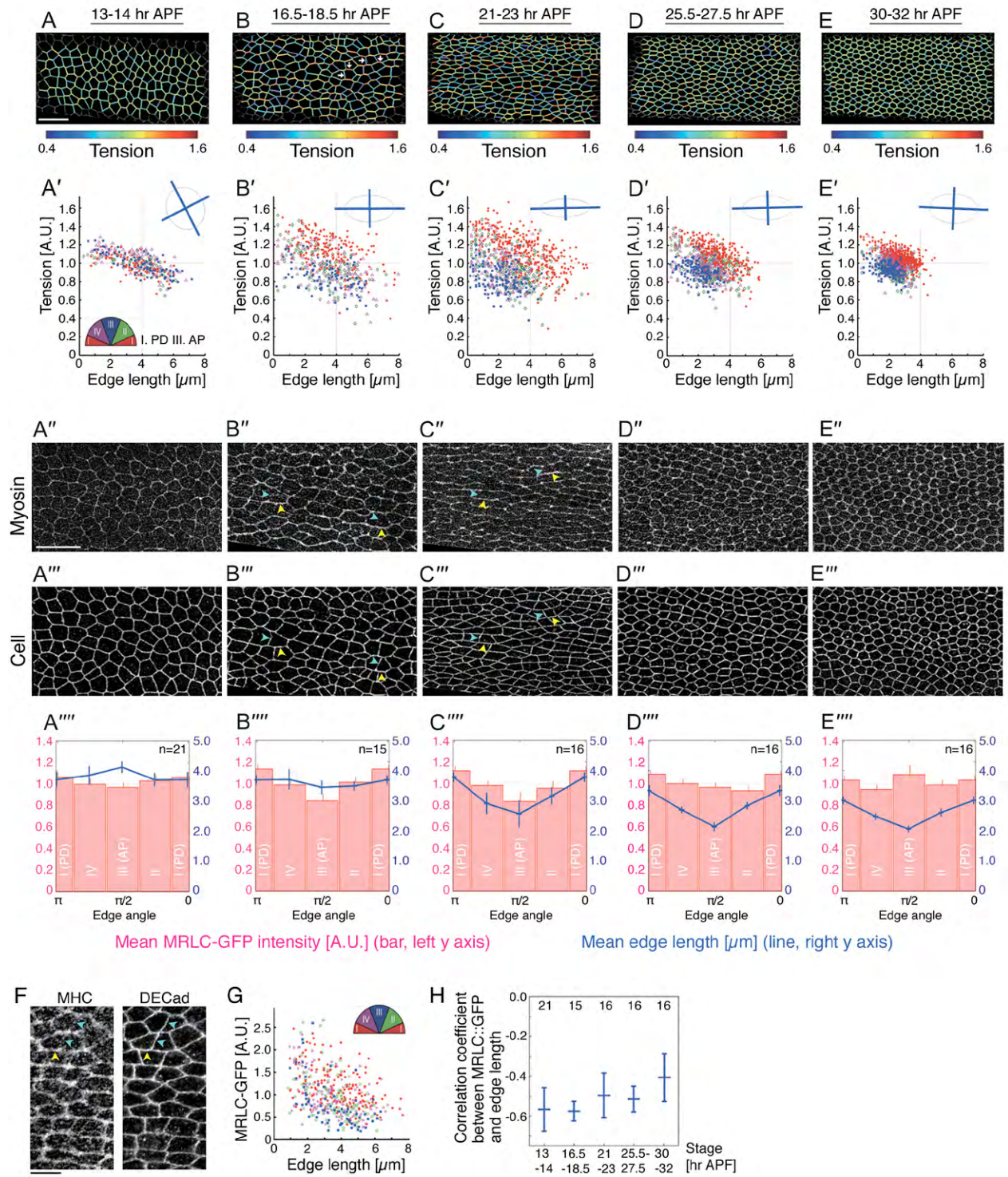


Fig. S2. Developmental changes in the distribution of inferred tension and the myosin subunit in the wing.

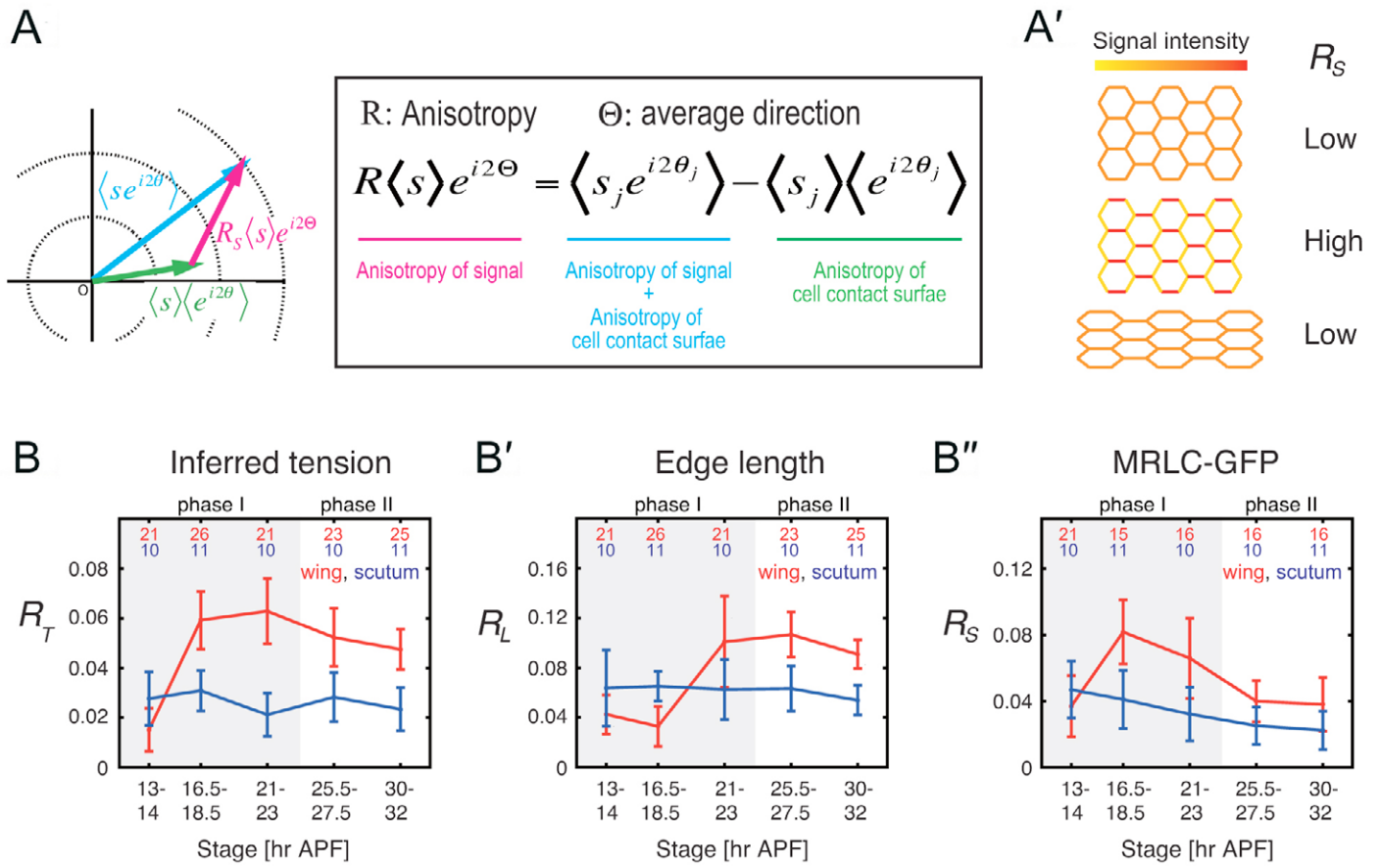


Fig. S3. Statistical analysis of the angular bias of inferred tension, edge length and MRLC signal intensity.

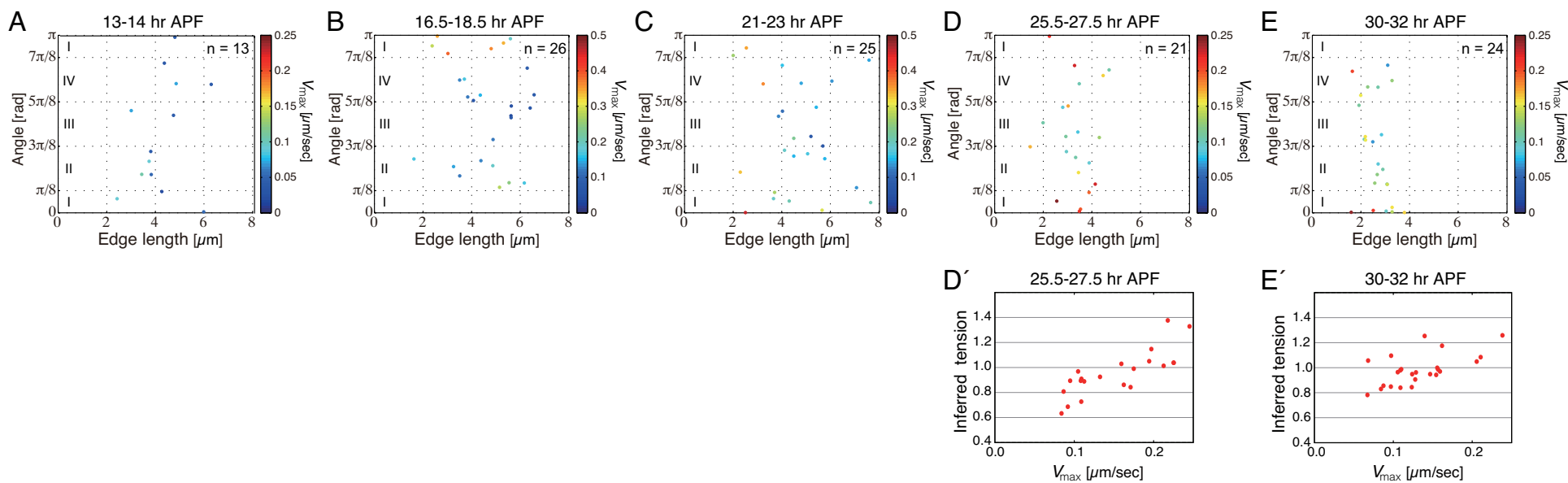


Fig. S5. Cell junction tension measured by response to laser ablation of single cell contact surface.

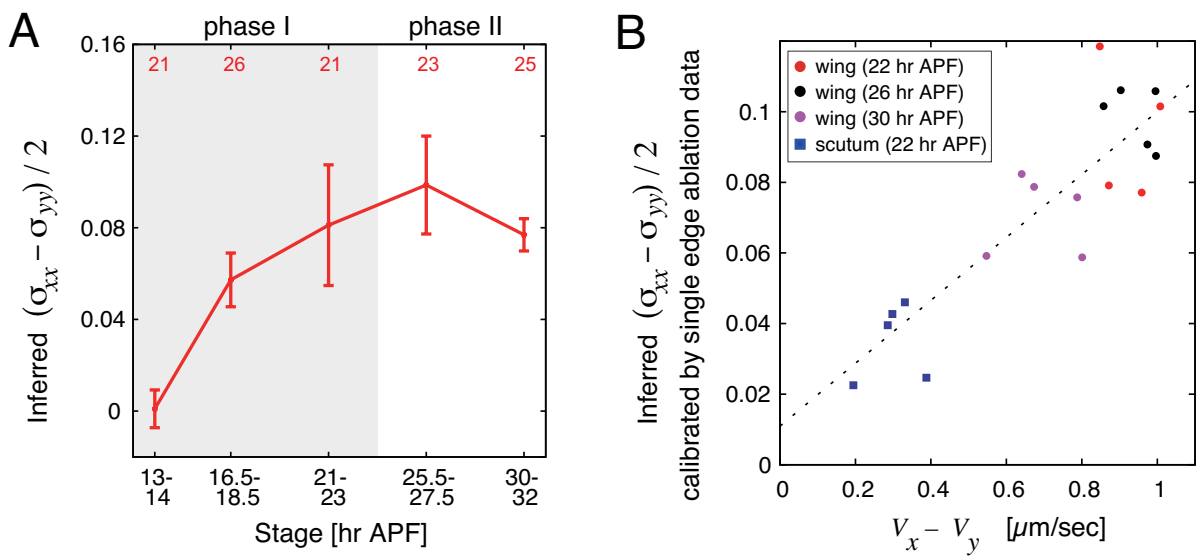


Fig. S6. Developmental changes in the anisotropy of global stress.

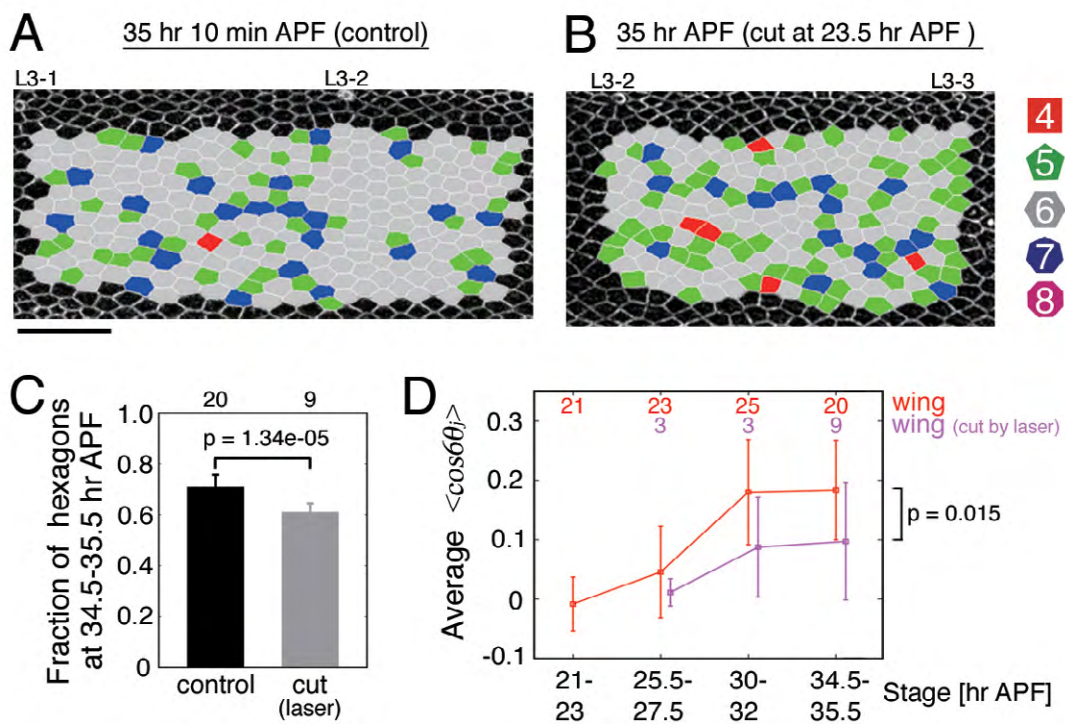


Fig. S7. Anisotropic stress promotes hexagonal packing.

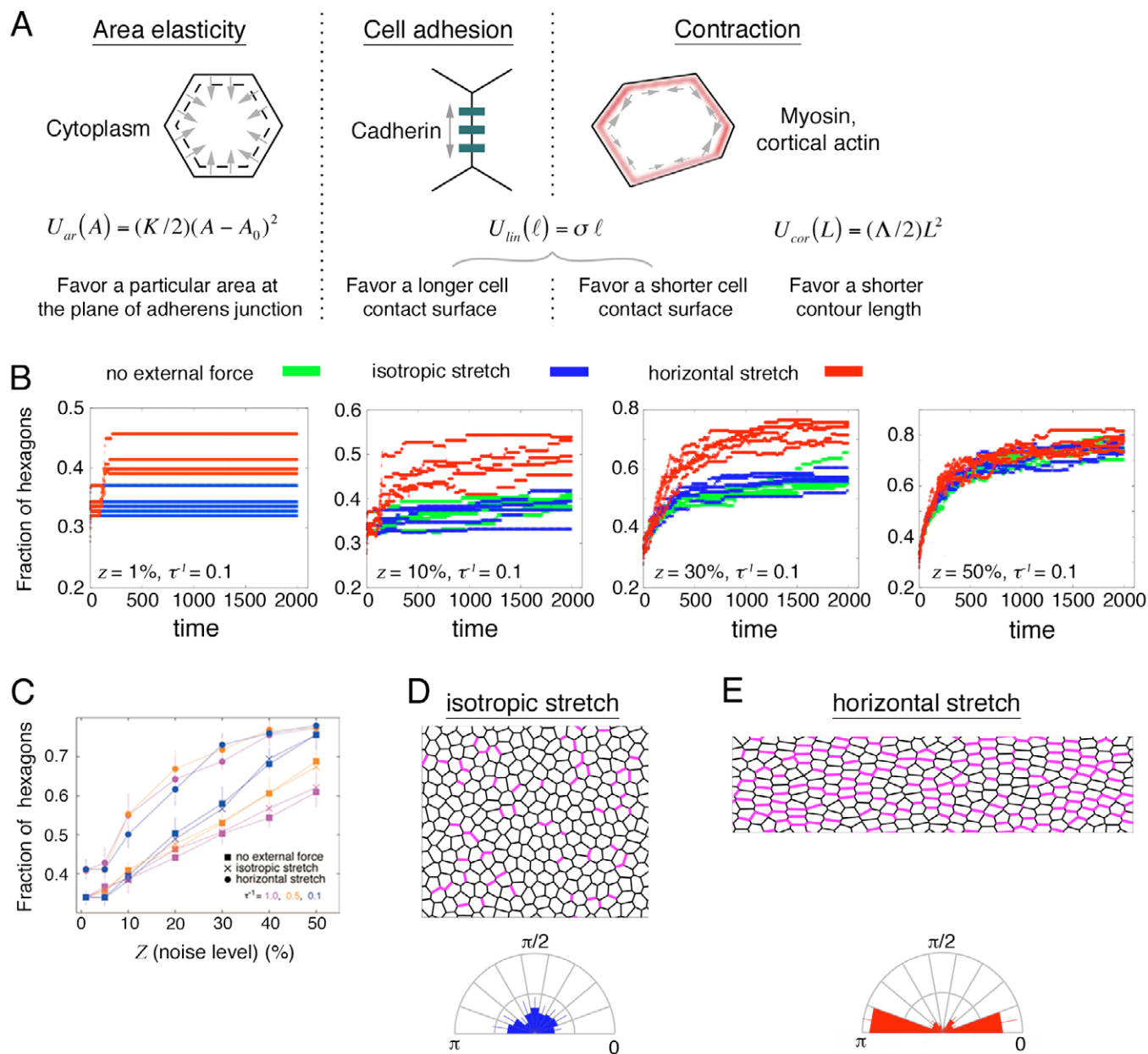


Fig. S8. Directional bias in stress is crucial for hexagonal packing in a numerical simulation of cell rearrangement.

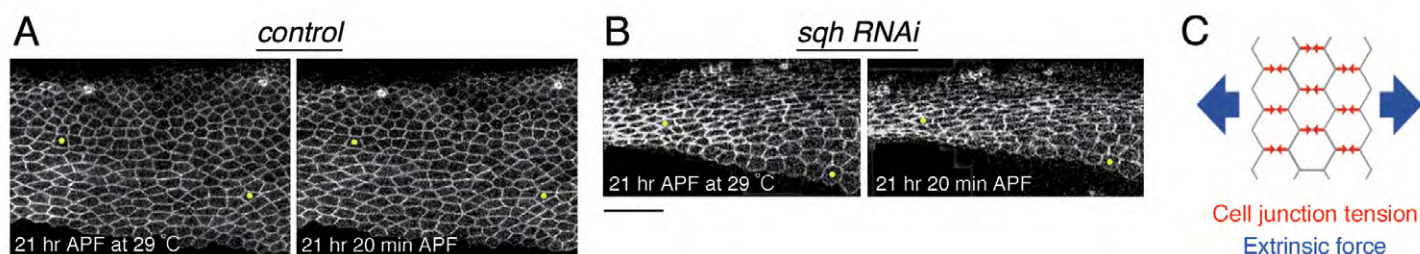


Fig. S9. The RNAi against *sqh* results in the excess shear deformation of wing cells.

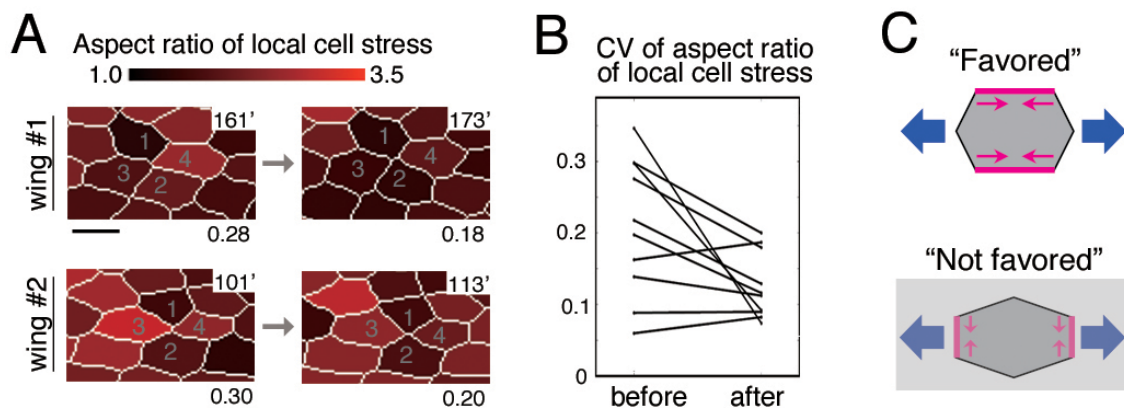


Fig. S10. Temporal changes in the anisotropy of local cell stress during hexagonal cell packing.

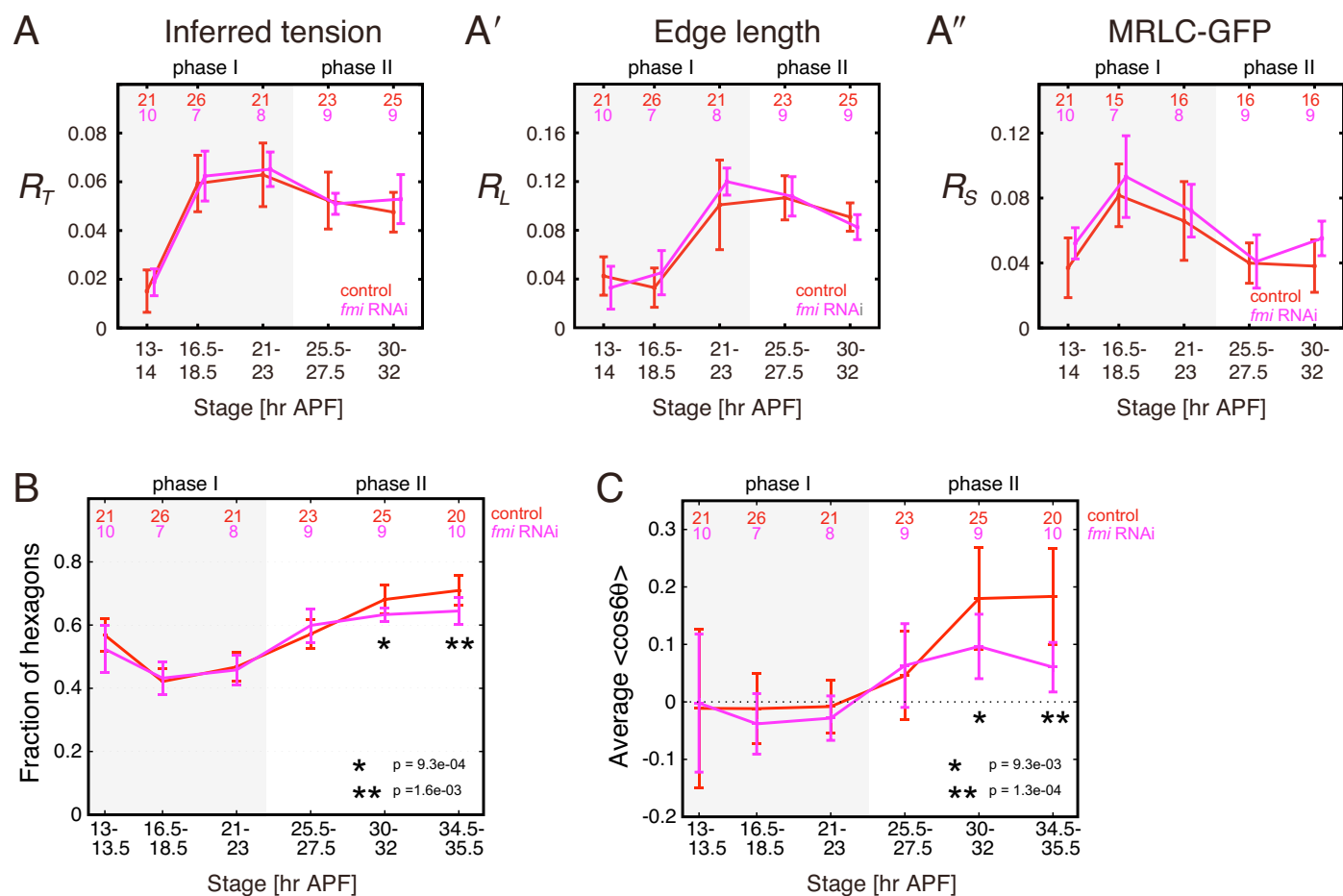


Fig. S11. In *flamingo* (*fmi*) RNAi wing, hexagonal packing proceeded normally until 27.5 h APF, but was disrupted afterwards.

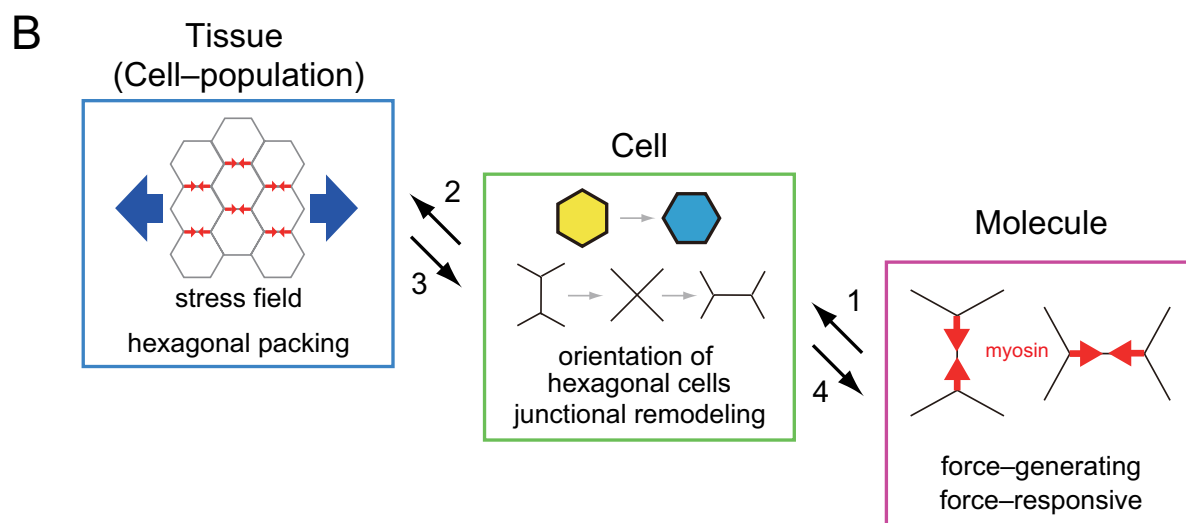
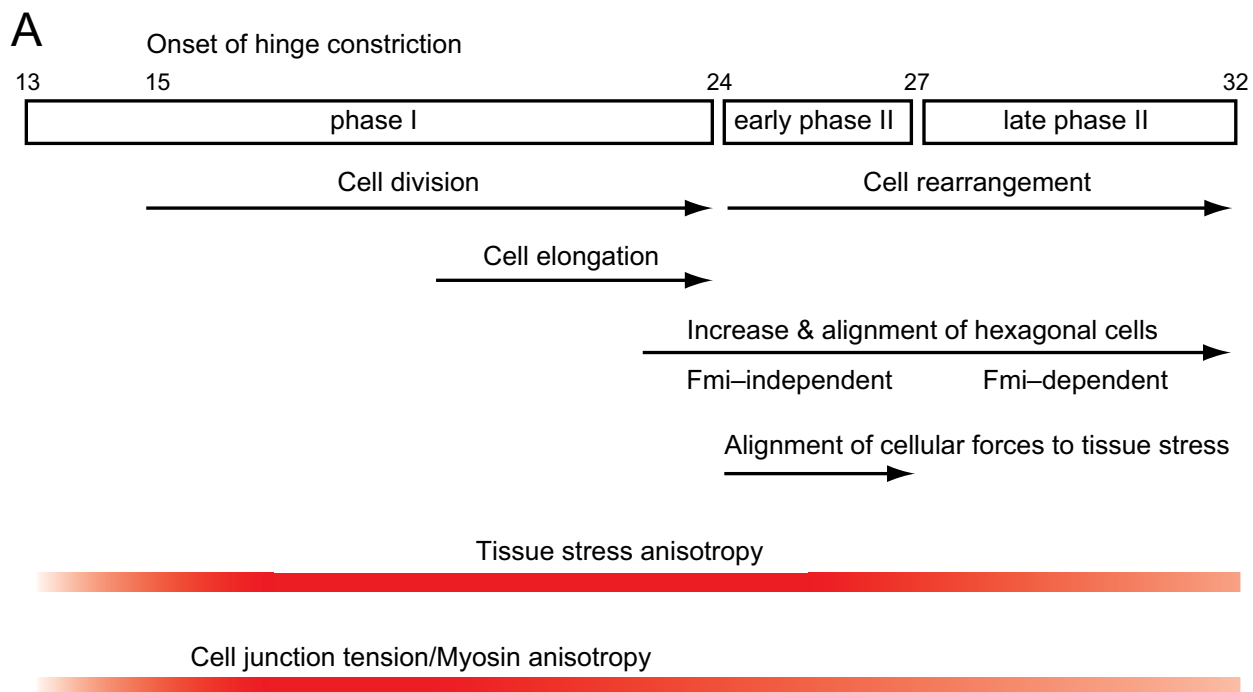


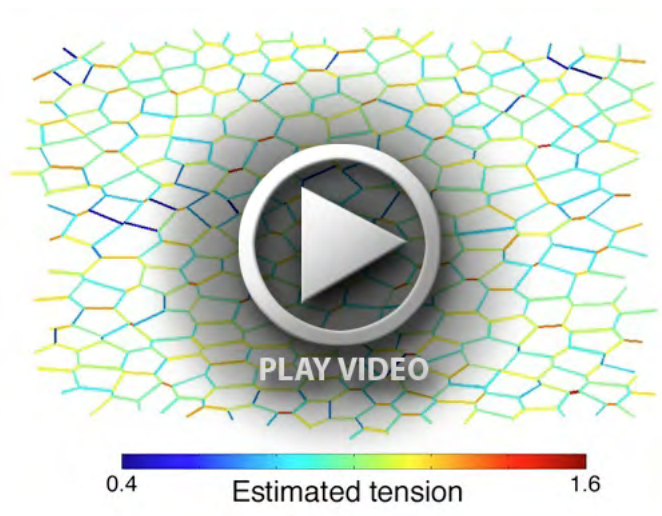
Fig. S12. Summary of tissue mechanics and cell-level dynamics that underlie hexagonal cell packing.



Movie 1. Ablation of a group of cells in the wing. A wing at 22 hours APF. Anterior is up and proximal is left. Cells at the center were ablated. The anisotropic extension of cell group contour confirmed the PD bias of global stress in the wing. Time label of the movie is: 14", -4", 4", 14", 24", ... , 214" (laser irradiation was at 0 seconds). The fly genotype is *DEcadherin-GFP* knock-in. Scale bar: 20 μm .



Movie 2. Ablation of a group of cells in the scutum. A scutum at 22 hours APF. Anterior is left. Cells at the center were ablated. Note that the anisotropy in the outward velocity of cells was smaller in the scutum than in the wing (compare Movies 1 and 2). The time label of the movie and fly genotype are as described in the legend of Movie 1. Scale bar: 20 μm .



Movie 3. Temporal dynamics of the inferred tensions. Time-lapse images were taken from 23.5-30.5 hours APF, and data from 25-26 hours APF were extracted at 3-minute intervals. The arrowheads and arrows point to the AP and PD edges, respectively. The fly genotype is as described in the legend of Fig. 1.

Appendix 1 by Sugimura and Ishihara.

§1. Force-inference method

1-A Force inference of pressures and tensions

The algorithm for inferring mechanical forces in a tissue was reported by Ishihara and Sugimura, 2012. In the method, an input is a segmented image of epithelial tissue represented by polygonal tile. Deviations from 120° angles between cell contact surfaces indicate heterogeneities in tensions and pressures, which can be found by solving a linear inverse problem (it is underdetermined, but can be solved under reasonable physical assumptions such as positivity of cell junction tensions). The difference of pressures among cells (ΔP_i) and tensions along cell contact surfaces (T_{ij}) are inferred up to a scaling factor; the estimated tensions and pressures are related to true ones as $\Delta P_i = cP_i^{true} + P_0$ and $T_{ij} = cT_{ij}^{true}$, where c is a scaling factor and P_0 is the baseline value of the pressure. P_0 is set so that the sum of ΔP_i is zero. Scaling factor c is set to satisfy that the average of estimated tensions is unity. In the developmental stages analyzed in this study, the average V_{max} of the vertices after cutting single cell contact surface did not change extensively; the average V_{max} was $0.153 \pm 0.054 \mu\text{m/sec}$ at 25.5–27.5 h APF ($n = 21$) and $0.132 \pm 0.044 \mu\text{m/sec}$ at 30–32 h APF ($n = 24$) (Fig. S5D1, E1).

1-B Global tissue stress and local cell stress

Global (tissue) stress tensor \mathbf{N} is given by the following matrix that integrates all cell pressures and tensions (see Fig. 1E for schematic representations) (Batchelor, 1970; Ishihara and Sugimura, 2012).

$$N_{\mu\nu} = \left[-\sum_{i \text{ cell}} A_i P_i \delta_{\mu\nu} + \sum_{\langle ij \rangle \text{ edge}} T_{ij} \frac{l_{ij}^\mu l_{ij}^\nu}{\|l_{ij}\|} \right] / \sum_{i \text{ cell}} A_i$$

Here, (μ, ν) are indices for (x, y) and $\delta_{\mu\nu}$ is Kronecker's delta. A_i is the area of the i th cell in the plane of the adherens junction, and $l_{ij} = (l_{ij}^x, l_{ij}^y)$ is a vector representation of the edge shared by the i th and j th cell. The global stress tensor is symmetric and thus is represented as a stress ellipse (insets in Figs. 2A3–C3, 4A3–C3).

We defined the local cell stress tensor by $N_{\mu\nu}^i = (-\Delta P_i A_i \delta_{\mu\nu} + \sum_j T_{ij} l_{ij}^\mu l_{ij}^\nu / \|l_{ij}\|) / A_i$ for individual cells (Ishihara and Sugimura, 2012) (see Fig. 1E for schematic representations). i is the index of the cell, A_i and ΔP_i are the area and the estimated relative value of the cell pressure, respectively, and T_{ij} is the estimated tension of cell contact surface between the i th and neighboring j th cell. Vector $\mathbf{l}_{ij} = (l_{ij}^x, l_{ij}^y)$ represents the relative position of two endpoints of the cell contact surface, and $\|l_{ij}\|$ is its length. μ and ν are indices of x and y . \sum_j represents taking the summation on the cell contact surfaces between the i th and adjacent cells. The obtained tensors are represented by cross symbols for respective cells. Anisotropy of local stress is measured by $a - b$ or a/b , where a and b are eigenvalues of the local cell stress tensor. The direction of global stretch is obtained by the eigenvector of the global stress tensor. Local cell stress along the global stress direction of the tissue is measured from the local cell stress tensors and the direction of global stretch.

§2. Numerical simulation

2-A Implementation of numerical model

Here we describe details of implementations of the numerical simulations. To simulate rearrangement of cells, we employed a vertex model with the following form for potential energy (Honda, 1983; Graner and Sawada, 1993; Ouchi et al., 2003; Mofrad and Kamm, 2006; Farhadifar et al., 2007; Käfer et al., 2007; Lecuit and Lenne, 2007; Rauzi et al., 2008):

$$U(\{\mathbf{x}_i\}, \lambda_x, \lambda_y) = U_0(\{\mathbf{x}_i\}) - \lambda_x T_x(t) - \lambda_y T_y(t), \quad (\text{eq. S2-1})$$

$$U_0(\{\mathbf{x}_i\}) = \sum_{i:\text{cell}} U_{\text{ar}}(A_i) + \sum_{[ij]:\text{edge}} U_{\text{lin}}(l_{ij}) + \sum_{i:\text{cell}} U_{\text{cor}}(L_i). \quad (\text{eq. S2-2})$$

A_i and L_i represent the area and peripheral length of the i th cell at the plane of the adherens junction, respectively. l_{ij} is the length of the contact surface between the i th and j th cells. A_i , L_i , and l_{ij} are determined by positions of the vertices $\{\mathbf{x}_i\}$ which define the geometry of cells. In eq. S2-2, the first term represents the area elasticity of a cell and is given by $U_{\text{ar}}(A) = (K/2)(A - A_0)^2$. The second term $U_{\text{lin}}(l) = \sigma l$ represents line tension (sum of cell adhesion and contracting force), and the third term $U_{\text{cor}}(L) =$

$(\Lambda/2)L^2$ represents cortical elasticity (Fig. S8A). In eq. S2-1, tissue stretch is introduced with the last 2 terms (Andersen, 1980; Frenkel and Smit, 2001), where λ_x and λ_y are new variables for parameterizing the system size as $L_x = \lambda_x L_x^0$ and $L_y = \lambda_y L_y^0$. $T_x(t)$ and $T_y(t)$ are applied stresses along the x - and y -axes, respectively. The ordinary differential equations to be solved are derived as follows.

$$\left\{ \begin{array}{l} \frac{dx_i}{dt} = -\lambda_x^2 F_i^x + \frac{T_x - \hat{T}_{xx}}{\lambda_x} x_i \\ \frac{dy_i}{dt} = -\lambda_y^2 F_i^y + \frac{T_y - \hat{T}_{yy}}{\lambda_y} y_i \\ \frac{d\lambda_x}{dt} = T_x - \hat{T}_{xx} \\ \frac{d\lambda_y}{dt} = T_y - \hat{T}_{yy} \end{array} \right. \quad (\text{eq. S2-3})$$

Here, \mathbf{F} is given by $-\partial U_0/\partial \mathbf{X}$ and $\hat{\mathbf{T}}$ is given by the following equation.

$$\hat{T}_{\mu\nu} = \sum_{i:\text{cell}} K(A_i - A_0)A_i + \sum_{[ij]:\text{edge}} \left(\sigma_{ij} + \Lambda(L_i + L_j) \right) \frac{l_{ij}^\mu l_{ij}^\nu}{\|\mathbf{l}_{ij}\|} \quad (\text{eq. S2-4})$$

With these equations $dU/dt \leq 0$ is assured when $\mathbf{T}(t) = (T_x(t), T_y(t))$ is constant. In the final steady state, $\mathbf{F}_i = 0$ for all i and $\mathbf{T} = \hat{\mathbf{T}}$ were satisfied as expected. In this implementation, introduced variables λ_x and λ_y that involve the global geometry of the system have no intuitive physical interpretation, but this methodology is widely used due to their technical advantages for simulating the dynamics under the specified stress environment with the periodic boundary condition (Frenkel and Smit, 2001).

In addition, fluctuation is included into the simulations so that the system is not trapped in a local minimum. One of the convenient ways is to add noise terms to line tension in the following form:

$$\dot{\sigma}_{ij} = -\tau^{-1}(\sigma_{ij} - \sigma_0) + z\sigma_0\sqrt{2/\tau}\xi_{ij}(t) \quad (\text{eq. S2-5})$$

Here, $\xi_{ij}(t)$ represents white Gaussian noise with $\langle \xi_{ij}(t) \rangle = 0$ and $\langle \xi_{ij}(t)\xi_{kl}(t') \rangle = \delta_{ij,kl}\delta(t - t')$. σ_{ij} fluctuates around its average σ_0 . τ determines the time scale of the fluctuation, and z controls its magnitude as $z = \langle |\sigma_{ij} - \sigma_0| \rangle / \sigma_0$.

The stochastic differential equations were numerically solved where junctional remodeling (T1 process) was allowed. To simulate the process of cell rearrangement without an extrinsic force (Fig. 3H, upper left), both $T_x(t)$ and $T_y(t)$ were set to 0.10 (an offset value) for all t . For the isotropic stretch (Fig. 3H, upper right), both $T_x(t)$ and $T_y(t)$ were set to 0.10 for $0 < t < 50.0$, and then were increased rapidly according to $T_x(t) = T_y(t) = 0.10 + 0.05 \times (t - 50.0)$ until they reached $T_x(t) = T_y(t) = 0.20$ at $t = 70.0$, and were constant afterward. For the anisotropic stretch along the x -axis (Fig. 3H, below), $T_y(t) = 0.10$ for all t and $T_x(t)$ was set as for the isotropic stretch condition.

Among the parameters of the potential U_0 , the values of K and A_0 are arbitrary by choosing the proper scales for physical dimensions (length and force); they were set as $K = 100.0$ and $A_0 = 1.0/256.0$ for this study. In the model, as the derivative of U_{cor} with respect to l shows, the coefficient of the quadratic term Λ is responsible for the length dependence of the tension at an edge. We found that Λ should be finite positive to reproduce the experimentally observed negative correlation between tensile force and edge length in the numerical simulations (Rauzi et al., 2008). In Figs. 3H, I, S8, we set σ_0 and Λ to $\tilde{\sigma}_0 = \sigma_0 / KA_0^{3/2} = 0.12$ and $\tilde{\Lambda} = \Lambda / KA_0 = 0.04$, as previously reported for the *Drosophila* wing disc, to reproduce the observed distribution of n -sided polygons and their areas after cell division (Farhadifar et al., 2007). Using these values, edge length and tension had a reasonable negative correlation.

Eventual fractions of hexagonal cells were nearly same for the 3 conditions at large and slow noise ($z = 50\%$ and $\tau^{-1} = 0.1$ in Fig. S8C). However, in most of the parameter regions examined, the eventual fraction of hexagonal cells under horizontal stretch was significantly larger than that under isotropic stretch (Figs. 3H–J, S8B). In addition, parameter dependence on τ differed among the 3 conditions; with large z , the fraction of hexagonal cells under no or isotropic stretch depended on τ (squares and crosses in Fig. S8C), whereas that under horizontal stretch did not (circles in Fig. S8C).

2-B Changes in cell shapes

Deformation of a tissue consists of a change in the shapes of constitutive cells and/or cell-cell intercalations (Blanchard et al., 2009). At an early phase of the simulations, application of isotropic or horizontal stretch triggered expansion or directional elongation of the cells, respectively (see $t = 50$ – 250 in Fig. 3H, upper right and below). Under an isotropic stretch, expansion of the cells reached a plateau due to their area elasticity, while cell intercalation among the cells was not biased and newly formed cell-cell surfaces were distributed isotropically (Fig. S8D). Therefore, the shape of the entire tissue changed only slightly between $t = 250$ and 2000 (Fig. 3H, upper right). On the other hand, under a horizontal stretch, biased cell intercalation caused formation of new cell-cell surfaces in the horizontal direction (Fig. S8E). Elongation of the constituent cells after $t = 250$ was not evident; hence, the biased intercalations were responsible for horizontal elongation of the tissue at this phase (see $t = 250$ – 2000 in Fig. 3H, below).

2-C Numerical Simulation with biased tensile parameter

Numerical model with biased tensile parameter was simulated as follows (Fig. 6A2). The model is obtained by replacing the line tension parameter σ in (eq. S2-2) by $\sigma (1 - \mu \cos 2\theta)$, where μ represents the magnitude of anisotropy. θ is the direction of the cell contact surface, thus the vertical contact surfaces in the figure have larger tension than horizontal ones. The system was under the isotropic pressure environment and we set $T_x = T_y = 0.10$. Λ and μ are controlled to obtain the results shown in Fig. 6B–D. The other parameters are set the as same as those described in §2-A.

In both tissue stretch and biased tensile parameter models, the anisotropy of cell shape (R_T) correlated less with the fraction of hexagonal cells than the orientation of cell contact surface ($\langle \cos 6\theta_i \rangle$) did (Fig. 6B–D). Therefore, although wing cells are elongated along the PD axis by the hinge constriction before reordering cell packing (~ 24 h APF) (Fig. 2A1, 2D2), it is suggested that cell elongation affects hexagonal cell packing less significantly than alignment of hexagonal cells.

Supplemental References

Andersen, H. C. (1980). Molecular-Dynamics Simulations at Constant Pressure and-or Temperature. *Journal of Chemical Physics* **72**, 2384-93.

Blanchard, G. B., Kabla, A. J., Schultz, N. L., Butler, L. C., Sanson, B., Gorfinkiel, N., Mahadevan, L. and Adams, R. J. (2009). Tissue tectonics: morphogenetic strain rates, cell shape change and intercalation. *Nat Methods* **6**, 458-64.

Frenkel, D. and Smit, B. (2001). Understanding molecular simulation: From Algorithms to Applications, San Diego: Academic press.

Gubb, D., Green, C., Huen, D., Coulson, D., Johnson, G., Tree, D., Collier, S. and Roote, J. (1999). The balance between isoforms of the prickly LIM domain protein is critical for planar polarity in Drosophila imaginal discs. *Genes Dev* **13**, 2315-27.

Ma, D., Yang, C. H., McNeill, H., Simon, M. A. and Axelrod, J. D. (2003). Fidelity in planar cell polarity signalling. *Nature* **421**, 543-7.

Matakatsu, H. and Blair, S. S. (2004). Interactions between Fat and Dachshous and the regulation of planar cell polarity in the Drosophila wing. *Development* **131**, 3785-94.